

Temperature dependence of single-event transients in SiGe heterojunction bipolar transistors for cryogenic applications

Xiaoyu Pan(潘霄宇), Hongxia Guo(郭红霞), Yahui Feng(冯亚辉), Yinong Liu(刘以农), Jinxin Zhang(张晋新), Jun Fu(付军), and Guofang Yu(喻国芳)

Citation: Chin. Phys. B, 2023, 32 (**9**): 098503. DOI: 10.1088/1674-1056/acaa28
Journal homepage: http://cpb.iphy.ac.cn; http://iopscience.iop.org/cpb

What follows is a list of articles you may be interested in

Microstructure, optical, and photoluminescence properties of β-Ga_2O_3 films prepared by pulsed laser deposition under different oxygen partial pressures

Rui-Rui Cui(崔瑞瑞), Jun Zhang(张俊), Zi-Jiang Luo(罗子江), Xiang Guo(郭祥), Zhao Ding(丁召), and Chao-Yong Deng(邓朝勇)
Chin. Phys. B, 2021, 30 (**2**): 028505. DOI: 10.1088/1674-1056/abc164

Preparation of Ga_2O_3 thin film solar-blind photodetectors based on mixed-phase structure by pulsed laser deposition

Y M Lu(吕有明), C Li(李超), X H Chen(陈相和), S Han(韩瞬), P J Cao(曹培江), F Jia(贾芳), Y X Zeng(曾玉祥), X K Liu(刘新科), W Y Xu(许望颖), W J Liu(柳文军), D L Zhu(朱德亮)
Chin. Phys. B, 2019, 28 (**1**): 018504. DOI: 10.1088/1674-1056/28/1/018504

Synergistic effect of total ionizing dose on single event effect induced by pulsed laser microbeam on SiGe heterojunction bipolar transistor

Jin-Xin Zhang(张晋新), Hong-Xia Guo(郭红霞), Xiao-Yu Pan(潘霄宇), Qi Guo(郭旗), Feng-Qi Zhang(张凤祁), Juan Feng(冯娟), Xin Wang(王信), Yin Wei(魏莹), Xian-Xiang Wu(吴宪祥)
Chin. Phys. B, 2018, 27 (**10**): 108501. DOI: 10.1088/1674-1056/27/10/108501

Experimental and simulation studies of single-event transient in partially depleted SOI MOSFET

Wei-Wei Yan(闫薇薇), Lin-Chun Gao(高林春), Xiao-Jing Li(李晓静), Fa-Zhan Zhao(赵发展), Chuan-Bin Zeng(曾传滨), Jia-Jun Luo(罗家俊), Zheng-Sheng Han(韩郑生)
Chin. Phys. B, 2017, 26 (**9**): 098505. DOI: 10.1088/1674-1056/26/9/098505

Improved high-frequency equivalent circuit model based on distributed effects for SiGe HBTs with CBE layout

Ya-Bin Sun(孙亚宾), Xiao-Jin Li(李小进), Jin-Zhong Zhang(张金中), Yan-Ling Shi(石艳玲)
Chin. Phys. B, 2017, 26 (**9**): 098502. DOI: 10.1088/1674-1056/26/9/098502

Temperature dependence of single-event transients in SiGe heterojunction bipolar transistors for cryogenic applications

Xiaoyu Pan(潘霄宇)[1,2], Hongxia Guo(郭红霞)[2,†], Yahui Feng(冯亚辉)[3], Yinong Liu(刘以农)[1], Jinxin Zhang(张晋新)[4], Jun Fu(付军)[5], and Guofang Yu(喻国芳)[5]

[1] *The Key Laboratory of Particle and Radiation Imaging, Ministry of Education, Department of Engineering Physics, Tsinghua University, Beijing* 100084, *China*
[2] *State Key Laboratory of Intense Pulsed Radiation Simulation and Effect, Northwest Institute of Nuclear Technology, Xi'an* 710024, *China*
[3] *School of Material Science and Engineering, Xiangtan University, Xiangtan* 411105, *China*
[4] *School of Aerospace Science and Technology, Xidian University, Xi'an* 710126, *China*
[5] *School of Integrated Circuits, Tsinghua University, Beijing* 100084, *China*

(Received 21 September 2022; revised manuscript received 30 November 2022; accepted manuscript online 9 December 2022)

We experimentally demonstrate that the dominant mechanism of single-event transients in silicon-germanium heterojunction bipolar transistors (SiGe HBTs) can change with decreasing temperature from +20 °C to −180 °C. This is accomplished by using a new well-designed cryogenic experimental system suitable for a pulsed-laser platform. Firstly, when the temperature drops from +20 °C to −140 °C, the increased carrier mobility drives a slight increase in transient amplitude. However, as the temperature decreases further below −140 °C, the carrier freeze-out brings about an inflection point, which means the transient amplitude will decrease at cryogenic temperatures. To better understand this result, we analytically calculate the ionization rates of various dopants at different temperatures based on Altermatt's new incomplete ionization model. The parasitic resistivities with temperature on the charge-collection pathway are extracted by a two-dimensional (2D) TCAD process simulation. In addition, we investigate the impact of temperature on the novel electron-injection process from emitter to base under different bias conditions. The increase of the emitter–base junction's barrier height at low temperatures could suppress this electron-injection phenomenon. We have also optimized the built-in voltage equations of a high current compact model (HICUM) by introducing the impact of incomplete ionization. The present results and methods could provide a new reference for effective evaluation of single-event effects in bipolar transistors and circuits at cryogenic temperatures, and could provide a new evidence of the potential of SiGe technology in applications in extreme cryogenic environments.

Keywords: SiGe heterojunction bipolar transistors, pulsed laser, TCAD simulation, single-event transient

PACS: 85.30.Pq, 61.80.Az, 73.40.Lq, 75.40.Mg **DOI:** 10.1088/1674-1056/acaa28

1. Introduction

Along with the continuous drive to explore deep space, how to save fuel consumption and enhance payload has been an important concern for scientists. Fortunately, silicon-germanium heterojunction bipolar transistors (SiGe HBTs) with a wide operating temperature range and radiation resistance (even above the multi-Mrad total ionizing dose tolerance) make it possible to free electronic systems from the 'warm box' and reduce weight and energy consumption. Early SiGe prototypes are already flying in the International Space Station (ISS).[1]

However, SiGe devices are sensitive to single-event effects (SEEs), and effectively assessing their susceptibility to SEEs under extreme temperature conditions is still a critical issue that needs to be addressed.[2] According to existing research, there have been some valuable studies on the impacts of temperature on SEEs for different devices and ion types; for example, proton-induced SEU in SiGe digital logic,[3] the heavy ion- and pulsed laser-induced SET in a PIN Si epilayer,[4,5] and CMOS bulk technology over temperature.[6] This research has found that the dominant contributor to the temperature response is the variation of carrier mobility, with other factors neglected. The carrier mobility increases with decreasing temperature, which leads to higher transient amplitudes at cryogenic temperatures. However, the effect of incomplete ionization (hereafter abbreviated as i.i.) of impurities was not studied.

In the literature,[7] the inflection point (induced by the impurity's incomplete ionization below 130 K) of the collector/substrate (C/S) junction's transient peaks was found for the first time by TCAD simulation. However, there is no experimental evidence that the inflection point of transient peaks due to i.i. exists. What is more, the simulation LET is too small (only 0.01 pC/μm) to trigger the ions-hunt effect of the emitter/base/collector (E/B/C) stack, which is a common effect induced by space-heavy ions.[8]

In this work, we investigate the temperature dependence of the SET (especially the ion shunt effect when the initial electron-hole pairs' (EHPs') concentration exceeds the doping concentration of the intrinsic base) response in SiGe HBTs

†Corresponding author. E-mail: guohxnint@126.com
© 2023 Chinese Physical Society and IOP Publishing Ltd

by two-dimensional (2D) raster scanning with a well-designed cryogenic test system suitable for pulsed-laser simulation.

There are two main innovations of this paper. Firstly, the increase in carrier mobility at low temperatures (which is well known already) and the i.i. of impurities (this work provides new experimental evidence) conjointly determine the change in resistivity on the charge-collection pathway, ultimately leading to variations of the drift transient peak. Secondly, when the device under test (DUT) switches from the cut-off state to the turn-on state (or the forward-active bias), there is a novel electron-injection process from the emitter to the base, which will increase the total charge collection.[2] An optimized built-in voltage equation of the high current compact model (HICUM)[9] has been provided with consideration of the i.i. The present experimental results illustrate that this novel injection process will be suppressed with decreasing temperature. According to existing research, this temperature dependence hasn't been reported otherwise. More importantly, this work provides new evidence for the possibility of using SiGe HBTs at cryogenic temperatures outside the shielding 'warm box'.

2. Experimental and simulation details

2.1. Cryogenic system

As is well known, cryogenic temperature experiments are very difficult to conduct due to the long cooling times to reach a stable temperature and the need for a high vacuum environment to avoid frosting;[10] therefore, temperature-related experiments tend to be performed at temperatures near or above room temperature. When it comes to pulsed-laser experiments, things get even harder because of the very short working distance between the optical lens and the surface of the DUT (< 1 cm). It is also important to note that even a very small amount of water vapor residue can have a significant impact on the accuracy of optical experiments. For these reasons, very few pulsed-laser studies have been performed for cryogenic temperatures.

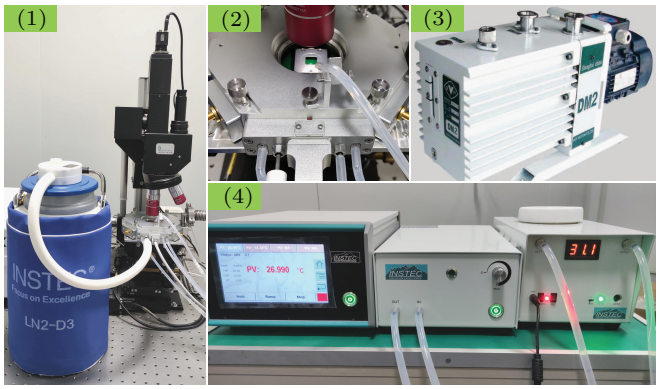


Fig. 1. The cryogenic system suitable for the pulsed-laser test contains (1) the laser system and the liquid nitrogen container; (2) a vacuum chamber with a hot and cold stage; (3) a vacuum pump; and (4) the precision temperature controller, liquid nitrogen cooling system, and the chillers.

Figure 1 shows the main components of our cryogenic system powered by INSTEC, which can provide a wide temperature range from −196 °C to +200 °C (with temperature stability better than ±0.1 °C). Before the experiment, the DUT was fixed directly on the silver stage with temperature sensors monitoring the real-time values. The vacuum pump usually requires 2–3 days (even longer) of continuous operation to remove most of the water vapor in the chamber, which is the key point for a laser test.

2.2. Radiation source

Nowadays, pulsed-laser systems are widely used as an important complement to high-energy ion accelerators for investigating SEEs.[11] This work was carried out at Northwest Institute of Nuclear Technology (NINT) by using the Nd:YAG laser system (powered by SPELS and EKSPLA), which can emit Gaussian laser beams with infra-red 1064 nm and visible 532 nm wavelengths. The single-photon energies of the 1064 nm laser and the 532 nm laser are $E_\gamma = 1.17$ eV and $E_\gamma = 2.33$ eV, respectively; both are above silicon's bandgap ($E_g = 1.12$ eV) at room temperature to induce inter-band single-photon absorption (SPA).[12] The pulse repetition rate is 1 kHz.

Since the absorption coefficient (α) of the 1064 nm laser in silicon decreases sharply as the temperature decreases,[13] it is unsuitable to use 1064 nm laser light to simulate heavy ions at low temperatures.[14] Fortunately, the 532 nm laser's α varies little with temperature, so the EHPs' generation rate changes a little with temperature just like the heavy ion's case.[15] In addition, the 1/e penetration length of the 532 nm laser beam is relatively short (about 1.25 μm), which makes it possible to focus on studying the ions-hunt effect of the HBT's E/B/C stack without considering the drift transient component from the C/S junction.

2.3. DUT description

The DUT is a low noise NPN SiGe HBT designed by the School of Integrated Circuits, Tsinghua University. The lithographic node (or the emitter size) of the device is 0.4 μm×20 μm, which is configured by an interdigital chip layout with a 4E5B2C structure, as shown in Fig. 2. Detailed information on the device is shown in Table 1.

Table 1. Technology parameters of the DUT.

Parameter	Value
Lithographic node (nm)	400
Peak DC current gain	150
Maximum collector current (mA)	30
Transition frequency f_T (GHz)	25
BV_{CBO} (V)	9
BV_{CEO} (V)	4.5
BV_{EBO} (V)	1

During the whole experiment, we kept the laser incident at the front side of the DUT for two main reasons: (1) decapping the backside package of the DUT can seriously affect its reliability; and (2) the 532 nm laser cannot penetrate the thick substrate layer to the sensitive volume. Since the sensitive area of the DUT is almost covered by a metal layer, only slits between the metal electrodes allow passage of the laser light into the semiconductor material. We selected a 50 μm×60 μm region, which covers all the sensitive volumes, and a 1 μm step size for the 2D raster measurements (in total, 3111 data points) to reduce errors caused by fluctuations in laser incidence position and the metal layer's blocking. The laser energy was fixed at 5 nJ to obtain more obvious transient signals that far exceed the testing noise floor.

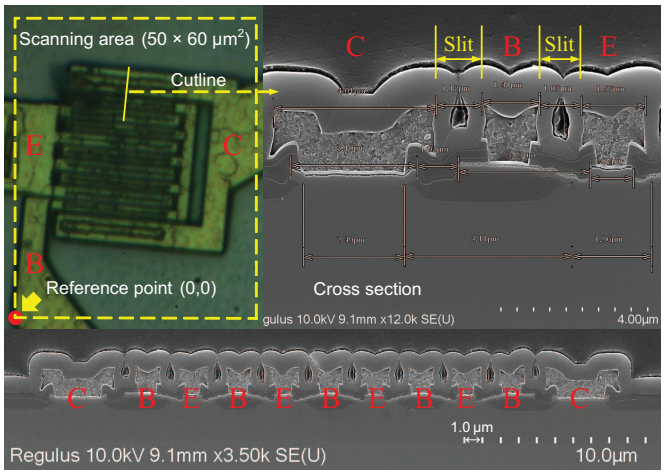


Fig. 2. The chip layout of the DUT (left) shows the 2D raster scanning area and the SEM figure (right) shows a cross-section by the cutline.

2.4. The 2D TCAD process model

To qualitatively analyze the underlying physical mechanism, we built a well-calibrated 2D TCAD process model, as shown in Fig. 3. One may notice that this is a simplified 1E2B2C structure, which gets better convergence at cryogenic temperatures, especially when the incomplete ionization model is activated (note that the convergence problem of three-dimensional (3D) simulation at cryogenic temperatures has always been a stumbling block to be solved). The whole 3D process model is also shown in our previous study.[16]

When the ion-shunt effect of the HBT's vertical E/B/C stack is triggered, a fast electron drift-collection process occurs from the emitter to the collector. Therefore, the resistance on this charge-collection pathway (shown in Fig. 3) can be approximated as a series connection of the vertical E/B/C stack's resistance (which includes $R_{\rm E}$, $R_{\rm B-V}$, and $R_{\rm C}$) and the lateral sub-collector's resistance, $R_{\rm SC}$. In particular, the $R_{\rm B-V}$ means vertical intrinsic base resistance rather than the lateral resistance used in common compact models. Figure 4 plots the doping concentration at the $Y = 0$ μm cutline.

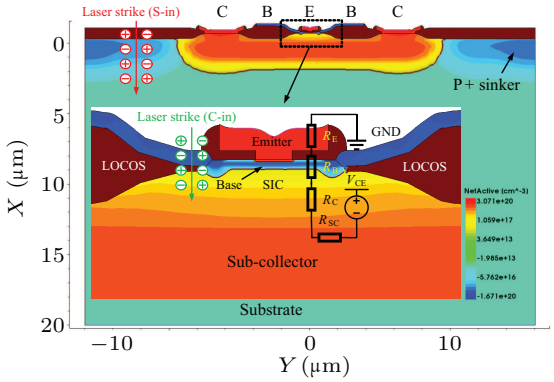


Fig. 3. The 2D process model of the DUT, with a zoomed-in view of the inside that shows the parasitic resistance of the E/B/C stack. The different laser normal strike positions, marked with S-in, denote the substrate incidence, and C-in denotes close to the emitter center incidence.

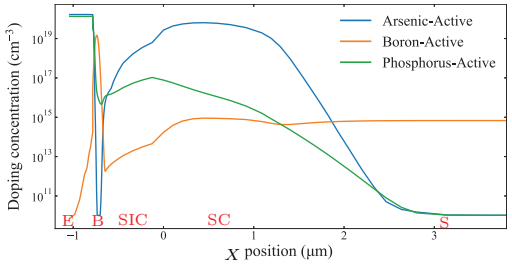


Fig. 4. The doping concentration was extracted from the 2D process model at the $Y = 0$ μm cutline.

2.5. Process simulation setup

To simulate the laser-induced SET, we introduced the SPA-induced EHPs' distribution to the TCAD process simulation by using the analytical calculation methods shown in our previous study.[16]

There are some related papers on how to calculate the profiles of EHPs generated by a pulsed laser,[17–20] such as Eq. (1), which shows the EHPs' generation rate at different positions:

$$g_{\rm las}(r,z,t) = \frac{2\alpha T_{\rm eff} E_{\rm L}}{\pi^{\frac{3}{2}}\omega_0^2 E_\gamma \tau}\frac{\omega_0^2}{\omega(z)^2}\,{\rm e}^{-\frac{2r^2}{\omega(z)^2}}\,{\rm e}^{-\alpha z}\,{\rm e}^{-\frac{t^2}{\tau^2}}, \quad (1)$$

where α is the linear absorption coefficient, $T_{\rm eff}$ is the effective transmission coefficient, $E_{\rm L}$ is the pulsed-laser energy, E_γ is the single-photon energy, r and z are the radial and axial propagation distance, respectively, ω and $\omega(z)$ are the $1/{\rm e}^2$ spot radius and contour after the wave has propagated a distance of z, respectively, and τ is the pulse duration.

Table 2. Laser simulation parameters.

Wavelength (nm)	Photon energy (eV)	Pulse duration (ps)	Absorption coefficient at 300 K ($\rm cm^{-1}$)	Spot radius (μm)
532	2.33	25	7989.2	5.6

Note in particular that the 532 nm laser's spot radius in Table 2 is 5.6 μm, which is far beyond the nominal value of 0.6 μm (given in Ref. [16]), and the reason is the presence of the 2 mm thick optical quartz window. As is shown in Fig. 5, the quartz window could bring two unfavorable effects: (1) it slows down the convergence of the laser beam due to the law of light refraction; and (2) it makes the CCD camera view unclear. To maintain the consistency of the pulsed-laser experiments, we first adjusted the X–Y–Z positioning platform in the Z-direction, so that the CCD camera could capture a relatively clear picture of the DUT's layout. We were then able to compare the Z-coordinates with and without the quartz window to estimate the actual focus position and spot radius (ω) by optical calculations.[11]

Fortunately, the larger beam spot size does not affect the validity of this work because the sensitive area with the metal layer's blocking is large enough (about 20 μm×20 μm, as shown in Fig. 2) and contains repetitive 4E5B2C structures. Anyway, in the future, we will further optimize this issue by using thinner quartz windows (about 1 mm) and adding a focusing lens.

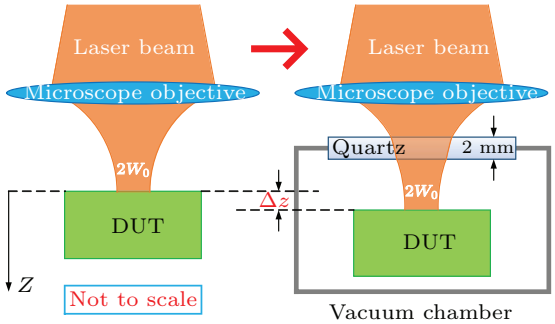


Fig. 5. Laser path diagram with (right) and without (left) temperature control (note that the impact of the quartz window on the focus location is shown in Δz).

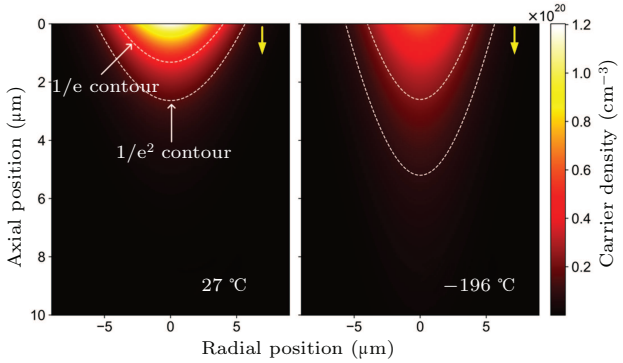


Fig. 6. The 2D profiles for the 532 nm laser-induced EHPs at 27 °C (300 K) and −196 °C (77 K) with 5 nJ laser energy. The yellow arrows indicate the direction of laser incidence and the white dashed lines indicate the 1/e and $1/e^2$ contours of the carrier density. The absorption coefficients at different temperatures used here are extracted from Ref. [27].

Finally, according to Eq. (1), and taking into account the laser parameters mentioned above, we can plot the initial EHPs' profiles, shown in a colormap in Fig. 6 ($T_{\text{eff}} = 1$)). As we can see, variation of the absorption coefficient α with temperature will slightly affect the initial carrier's distribution (CD) while keeping the total amount constant. For simplicity, we adopted the α at 300 K to generate the initial CD profiles at all simulation temperature points.

We can then simulate the SPA-induced SET by modifying the heavy ion GCs' model parameters in TCAD. Our previous study[16] shows this process in detail. In addition, to simulate the carrier freeze-out,[21] we activated the Philips unified mobility model (PHUMOB),[22,23] Canali velocity saturation model,[24] Slotboom bandgap narrowing model,[25] and the incomplete ionization model.[26]

3. Temperature dependence of the transient peak

3.1. The 2D raster scan measurement

There are two main reasons for conducting 2D raster scan testing: (1) to obtain the SET sensitivity distribution of the entire chip; and (2) when averaging the waveforms in the same region, the influence of fluctuations in the metal layer's blocking, and the laser incident position, the incident energy on the experimental results is reduced.

We set six temperature points at equal intervals (40 °C) from +20 °C to −180 °C by using the cryogenic system mentioned in Subsection 2.1. We also changed the bias conditions of the DUT at each temperature point, including the on-state (with $V_{\text{CE}} = 2$ V, $V_{\text{BE}} = 0.7$ V) and off-state (with $V_{\text{CE}} = 2$ V, $V_{\text{BE}} = 0$ V).

After 2D raster measurements, we statistically calculated the transient peaks and collected charges (CCs) at 3111 laser incident points for each temperature, as shown in the colormaps of Figs. 7 and 8. As can be seen, the presence of only one metal layer could also have a significant impact on SPA-induced transient peaks and CCs. The maximum values of both transient peaks and CCs are located in the area without a metal layer (the outside substrate region).

However, based on our previous studies,[16,28] the most sensitive volume for a SiGe HBT's SET should be the central interdigital structure (especially the emitter center normal incidence) if there is no metal layer. Therefore, we divided the scanning area into the center-incidence (C-in) region (red boxes in Fig. 7) and the substrate-incidence (S-in) region (white arrows in Fig. 8). The definitions here are the same as in Fig. 3.

In particular, the red boxes (10 μm×10 μm) in Fig. 7 are the central parts of the 4B5E2C interdigital region (20 μm×20 μm) considering the large 5.6 μm laser-spot radius. We then calculated the mean values of the SET waveforms in the C-in and S-in regions. As an example, the off-state's results are plotted in Fig. 9. One can see that the transient peaks firstly increase with decreasing temperature (a maximum increment of about 25%), and then decrease slightly from −140 °C to −180 °C for the C-in case. In this region, the fast drift current dominates the SET waveform.

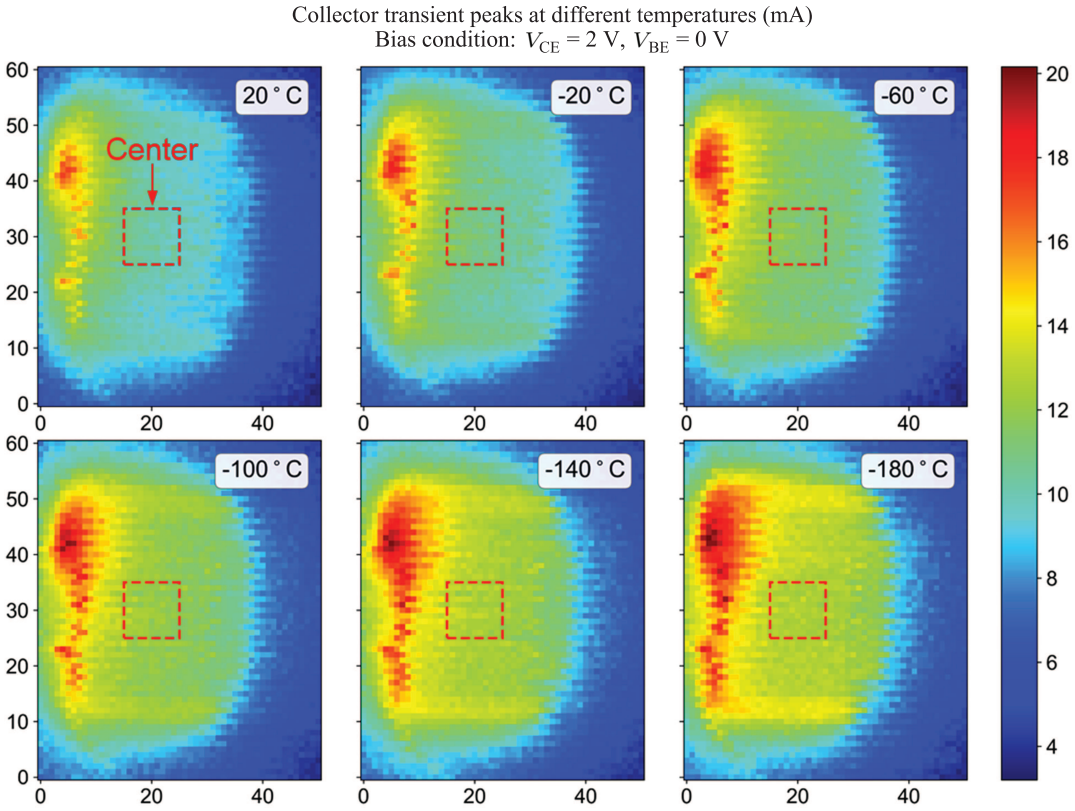


Fig. 7. The 2D raster measurements for the collector transient peaks at different temperatures. The red box illustrates the center-incidence (close to the emitter center) of the 4E5B2C structure with the metal layer's blocking.

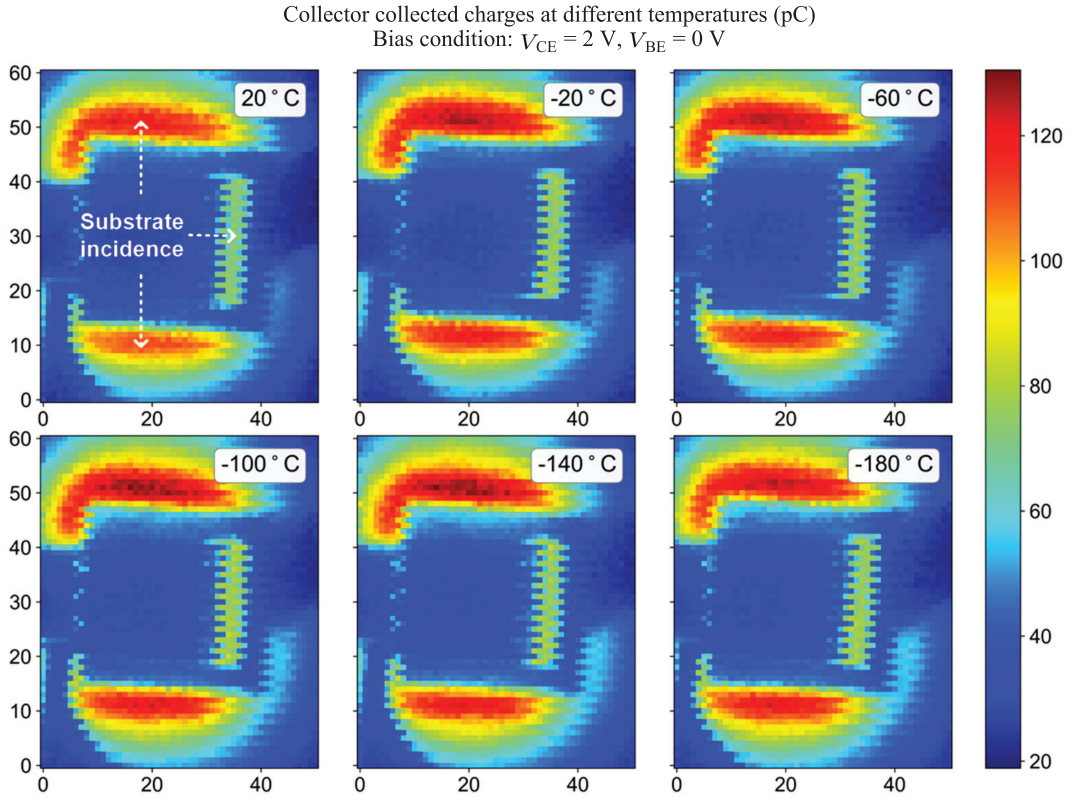


Fig. 8. The 2D raster measurements for the collector collected charges at different temperatures. The white arrows illustrate the substrate-incidence (outside the 4E5B2C structure) positions without the metal layer's blocking.

As a comparison, the transient peaks continue to slightly increase (a maximum increment of about 35%) for the S-in case because the dominant current is the diffusion current. For both cases, the full width at half maximum (FWHM) decreases with decreasing temperature and the total CCs show little change (as shown in Fig. 10). What is more, we can ob-

tain an estimate of the effective laser energy (0.15 nJ) and the surface LET value (28.37 pC/μm) of the C-in case.

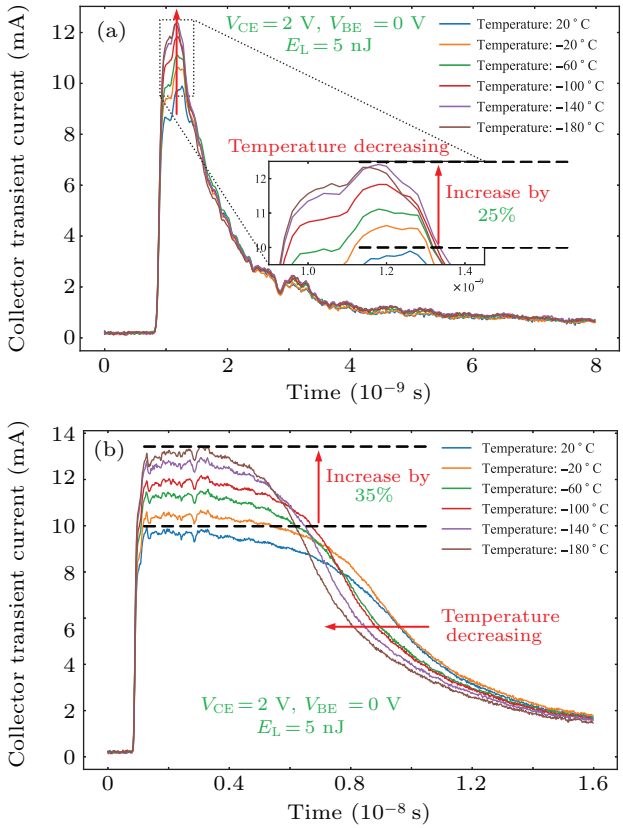


Fig. 9. Mean waveforms for the collector's SETs at different temperatures under (a) the C-in case and (b) the S-in case. The different time scales are shown right below.

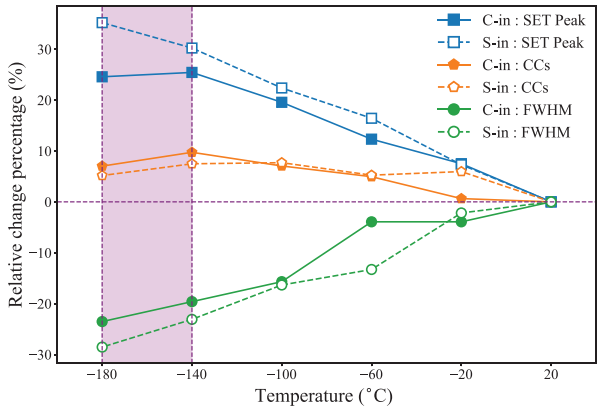


Fig. 10. Relative percentage change (relative to 20 °C) on the collector's SET peak, CCs, and FWHM under the C-in case and the S-in case (with $V_{CE}=2$ V, $V_{BE}=0$ V).

3.2. The 2D process simulation and analysis

In this paper, we have modified the TCAD parameter file of the heavy-ion model according to the analytical calculation results in Subsection 2.5 and have modified the simulation script file to simulate the pulsed laser penetrating a device structure based on the approach in our previous study.[16]

First, let us focus on the C-in case. Taking the transmission coefficient of the 2 mm thickness quartz window, the reflection of the DUT surface, and the blocking of the metal layer into account, we give a relatively rough estimated value of the effective transmission coefficient (in Subsection 2.5) based on the simulation results, here $T_{\rm eff}=0.1$.[29] What is more, we have set the laser incidence position exactly to the emitter center normal incidence (the most sensitive volume).

It should be noted that it is difficult to find the real laser incidence position precisely. And considering that the high concentration of carrier profiles generated by the 5 nJ laser energy is sufficient to trigger the ion-shunt effect, these assumptions for the laser incidence position and effective transmission coefficient $T_{\rm eff}$ are relatively reasonable, and do not affect the qualitative analysis and interpretation of the experimental phenomena in this paper. Figure 11 shows the SET simulation results in the off-state. The maximum value of the SET peak is around −160 °C, which is 23.7% higher than 20 °C and is similar to the testing results shown in Fig. 9(a). The difference in FWHMs and durations between the simulation and experimental results come from the 2D simplified 1E2B2C simulation structure and the parasitic parameters from our testing system.

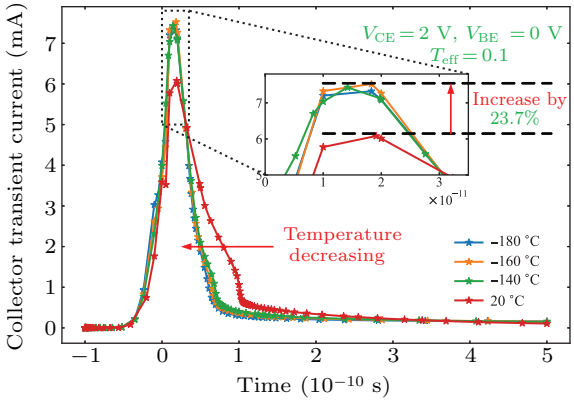


Fig. 11. The C-in (emitter center normal incidence) SET waveforms from the TCAD simulation at different temperatures.

As mentioned before, many previous studies have attributed the temperature dependence of SET to carrier mobility. Carrier freeze-out at low temperatures doesn't get enough attention. However, the TCAD simulation results in Ref. [7] have compared the SET's temperature response with and without considering the i.i. at low temperatures. The peak inflection was only observed at the C/S junction's transient component because the simulation LET is too small to trigger the ion-shunt effect.

The law of exponential variation of carrier mobility with temperature has been generally accepted for a long time. In the following, we focus on the i.i. of impurities at low temperatures. Taking the moderately doped intrinsic base as an example, we will introduce the ionization rate (IR) calculation process in detail. According to Altermatt's i.i. model[30,31] and the optimized compact model by Luo *et al.*,[32] the impurity states could be divided into the always completely ionized free-states (with the share of $1-b$) and partially ionized

bound-states (with the share of b), then the ionized acceptor's concentration is shown below:

$$N_{\rm A}^{-} = (1-b)N_{\rm A} + bN_{\rm A} \times f(E_{\rm A}), \tag{2}$$

where $N_{\rm A}$ is the doping concentration, and $f(E_{\rm A})$ is the probability of the acceptor energy level $E_{\rm A}$ being occupied by electrons

$$f(E_{\rm A}) = \frac{1}{1 + g_{\rm A} \exp \frac{(E_{\rm A} - E_{\rm F})}{kT}}, \tag{3}$$

with $g_{\rm A} = 2$ being a degeneracy factor for boron doping. Therefore, the IR with temperature could be found by

$$\begin{aligned} {\rm IR}(T) &= \frac{N_{\rm dop}^{-}(T)}{N_{\rm dop}} = (1-b) + b \times f(E_{\rm A}) \\ &= (1-b) + \frac{b}{1 + g_{\rm A} \exp \frac{E_{\rm dop}}{kT} \exp \frac{(E_{\rm V} - E_{\rm F})}{kT}}, \end{aligned} \tag{4}$$

where $E_{\rm V}$, $E_{\rm F}$, and $E_{\rm dop}$ are, respectively, the valence band level, Fermi level, and the acceptor's activation energy.

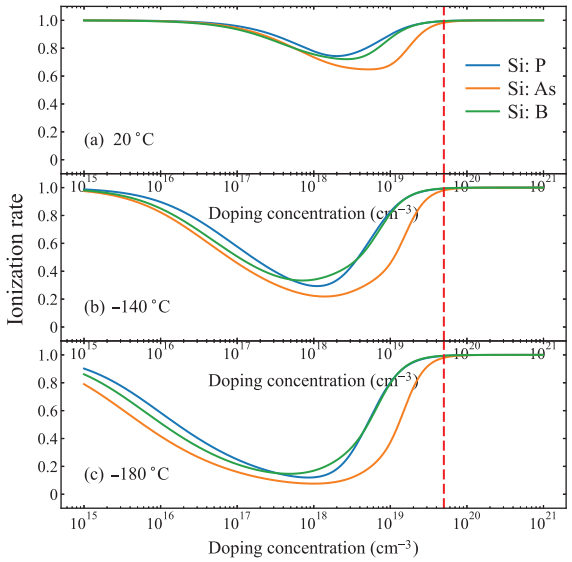


Fig. 12. The ionization rate (unit: one) versus doping concentration at different temperatures for phosphorus, arsenic, and boron doping.

Detailed parameter settings and descriptions can be found in Refs. [30–32] and will not be presented here one by one. Finally, we calculated the three dopants' ionization rates for the DUT, which are shown in Fig. 12. We can see that i.i. could occur even at room temperature when the doping concentration is close to the Mott (metal–insulator) transition.[33] What is more, the ionization rate will decrease significantly when the temperature changes from −140 °C to −180 °C for both less than and close to the Mott transition. The peak doping concentrations in the base and the selectively implanted collector (SIC) are about 1×10^{19} cm^{-3} and less than 1×10^{18} cm^{-3}, respectively (from Fig. 4), so these two moderate doping resistances ($R_{\rm B-V}$ and $R_{\rm C}$ in Fig. 3) are dominated by both mobility and impurity IRs. For heavily doped regions (above 5×10^{19} cm^{-3}) like the emitter and sub-collector (or n^{+} buried), the impurities are always completely ionized and the resistances ($R_{\rm E}$ and $R_{\rm SC}$ in Fig. 3) are controlled directly by the carrier mobility.

In addition, the SPA-induced high-density EHPs will also impact the local resistance on the charge-collection pathway because they can significantly change the free carriers' concentration. Therefore, we need to calculate the resistivity by considering both the electrons' and holes' mobilities and concentrations by using

$$\rho = \frac{1}{q(\mu_n n + \mu_p p)}, \tag{5}$$

where n and p are the electron and hole concentrations generated by both the intrinsic impurity's ionization and the radiation-induced ionization, and $\mu_{n,p}$ are the electron and hole mobility, respectively. As shown in Fig. 13, to qualitatively illustrate the relationship between the drift peak and resistivity, we extracted the resistivity values on the transient current pathway at the SET peak moments (around 20 ps) from the 2D process model. From −140 °C to −180 °C, $R_{\rm B-V}$ and $R_{\rm C}$ obviously increase and $R_{\rm E}$ and $R_{\rm SC}$ slightly decrease.

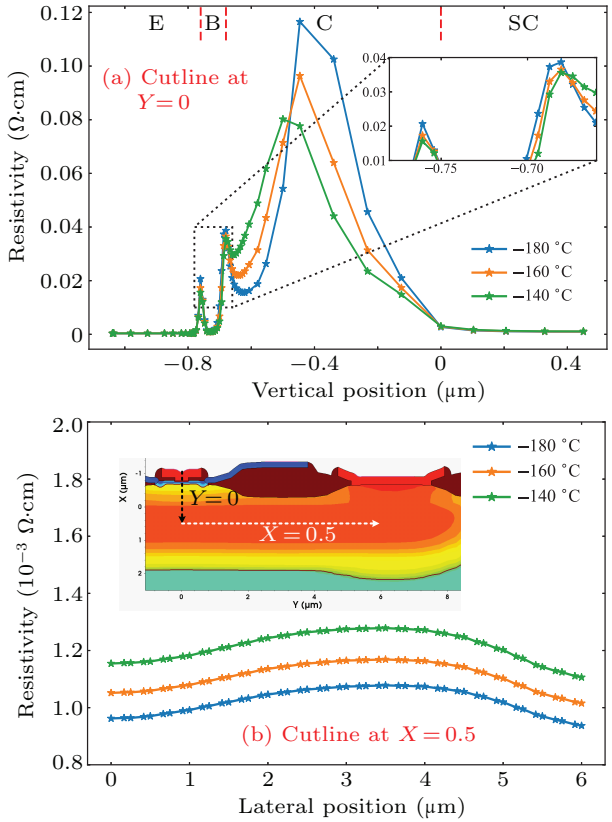


Fig. 13. Variation of resistivity (at 20 ps) with temperature at different positions: (a) cutline at $Y = 0$; (b) cutline at $X = 0.5$.

Finally, we should also consider the structural dimensions of different regions on the E/B/C stack to obtain series resistance (details in Fig. 3) other than resistivity. There are two competing mechanisms for the variation of the total series resistance with temperature: (1) the moderate doping base

(R_{B-V}) and lighter doping SIC (R_C) with relatively high resistivities (which increase as temperature decreases) and very small vertical size; and (2) the heavy doping sub-collector (R_{SC}) with lower resistivity (which drops along with temperature) and a much larger lateral size. In addition, the contribution of the emitter (R_E) to the total series resistance can be considered negligible because of its low resistivity and small vertical size.

Taking into account these two competing mechanisms, it is not surprising to see a shift in the total resistance on the charge-collection pathway, which finally leads to an inflection point in the transient peak. In future work, the coupling between the 3D structure size and charge distribution needs to be fully considered in the calculation of series resistance.

Next, we discuss the S-in case (in Figs. 3 and 8), which means that the pulsed laser strikes the outside substrate region without the metal layer. From the experimental results in Fig. 9(b), we can see that the transient peak continues to slightly increase as the temperature decreases. The reason for this is that the SET current for substrate-incidence is mainly the diffusion current, which is dominated by the ambipolar diffusion coefficient (D_a). For high-level injection (when EHPs' concentration is far beyond the background doping level, just like in this work), we could estimate D_a from the equation in Ref. [34]. From the exponential increase of mobility with decreasing temperature, the carrier mobility's variation will always dominate the bipolar-diffusion process.

4. Temperature dependence of the novel electron-injection process

4.1. Experimental and simulation results

During the 2D raster scan measurements, we also considered the impact of different bias conditions. We then found an important conclusion: that the novel electron injection from the emitter to the base will be suppressed at cryogenic temperatures. And this time, we will focus on the C-in case (emitter center strike) again.

By keeping all the experimental and simulation setups the same as in Section 3, we could obtain the collector transient currents with different bias conditions and temperatures, which are shown in Fig. 14. The transient peaks for both the experimental and simulation results show a similar pattern of variation. When it comes to the total CCs, the simulation results have amplified the changes in the experiments. This deviation comes from the difference between the 2D simulation and the actual 3D device structure as well as the accuracy of the TCAD physical model.

Nevertheless, we can conclude that the transient peaks and CCs at low temperatures remain stable under different bias conditions. There will also be more electron injection from the emitter to the base when the temperature increases.

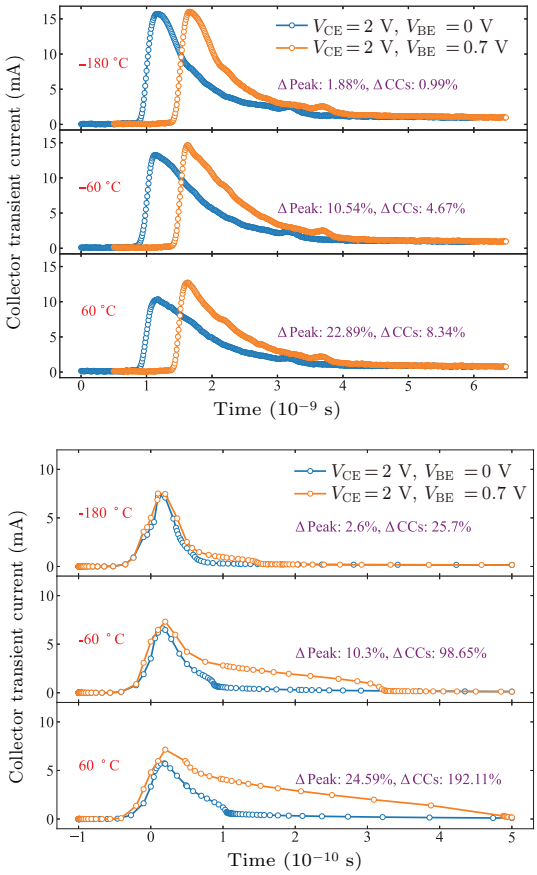


Fig. 14. Variation of collector transient currents with temperature under different bias conditions: (a) experimental waveforms (note that, to show the differences between waveforms more clearly, the waveforms are artificially shifted in the time axis.); (b) TCAD simulation waveforms. Note that all DC components have been filtered out here.

4.2. Theoretical analysis

There are few studies on the bias condition dependence of a SiGe HBT's SET. In the literature,[2] the conception of a 'novel collector-emitter diffusive component' was proposed after SET testing on a 9HP SiGe HBT. In this work, we call it the 'novel electron-injection process from emitter to base'. It should be noted that the 'electron' here indicates the laser-induced free electrons at the emitter. The conduction band electrons generated by intrinsic impurity ionizing mainly produce the DC component, which has been filtered out here.

As is shown in Fig. 15, this novel carrier injection is based on the principle that the positive bias voltage applied at the base lowers the potential barrier between the emitter and the base, thus allowing more electrons to cross (a diffusion-like process) the barrier layer to the base and eventually be collected by the collector terminal. Therefore, the temperature dependence of the E/B junction's potential barrier will dominate this electron-diffusion process.

The built-in voltage (V_{bi}) of the E/B junction is dominated by the material's lattice temperature and doping-dependent bandgap narrowing (BGN).[35] For silicon, the bandgap voltage (V_g) decreases as temperature increases, which could be

described by Eq. (6) (from the HICUM model[9])

$$V_{\rm g}(T) = V_{\rm g}(T_0) + k_1 \frac{T}{T_0} \ln\left(\frac{T}{T_0}\right) + k_2\left(\frac{T}{T_0} - 1\right), \tag{6}$$

where T is the nominal temperature 300 K (27 °C), and $k_1 = -0.025$ V and $k_2 = -0.053$ V are constant parameters.

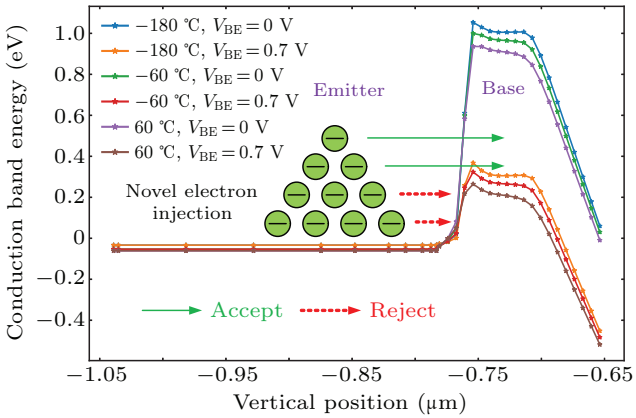


Fig. 15. Novel carrier injection schematic. Note: the variation of the conduction band energy near the emitter-base junction with temperature and bias is extracted from the 2D TCAD simulation results.

Considering the i.i. (detailed in Subsection 3.2), we have then optimized the built-in voltage as

$$V_{\rm bi}(T) = V_T \ln\left[\frac{N_{\rm D} N_{\rm A}^-(T)}{n_{\rm ie}^2(T)}\right], \tag{7}$$

where $N_{\rm D}$ is the donor concentration (complete ionization due to the high doping level) of the emitter, $N_{\rm A}$ is the ionized acceptor concentration of the base, V_T is the thermal voltage (kT/q), and $n_{\rm ie}$ is the effective intrinsic carrier concentration by considering the BGN's influence

$$n_{\rm ie}^2(T) = n_{\rm ie}^2(T_0)\left(\frac{T}{T_0}\right)^3 \exp\left[\frac{V_{\rm g}(T_0)}{V_{T0}} - \frac{V_{\rm g}(T)}{V_T}\right]. \tag{8}$$

Next, taking the i.i. into account, we could obtain the optimized built-in voltage in Eq. (9), and the last term shows the role of i.i. Eq. (10) illustrates the proportional relationship between the IR and ionized impurity concentration from Subsection 3.2.

$$\begin{aligned} V_{\rm bi}(T) \;=\; & V_{\rm bi}(T_0)\frac{T}{T_0} + V_{\rm g}(T) - V_{\rm g}(T_0)\frac{T}{T_0} \\ & - 3V_T \ln\left(\frac{T}{T_0}\right) - V_T \ln\left[\frac{N_{\rm A}^-(T_0)}{N_{\rm A}^-(T)}\right], \end{aligned} \tag{9}$$

$$\frac{{\rm IR}(T_0)}{{\rm IR}(T)} = \frac{N_{\rm A}^-(T_0)}{N_{\rm A}^-(T)}. \tag{10}$$

It should be noted that the reference bandgap voltage $V_{\rm g}(T_0) = 1.01$ V is the average bandgap voltage of the emitter and the base,[9] by considering the impact of the Ge mole fraction.

Using the equations above, we could calculate the built-in voltages of the E/B junction at different temperatures, as shown in Fig. 16. The built-in voltage of the E/B junction will increase as temperature decreases. And the simulation's built-in barrier's height is consistent with the analytical calculation results, which validate the effectiveness of our optimized built-in voltage calculation model.

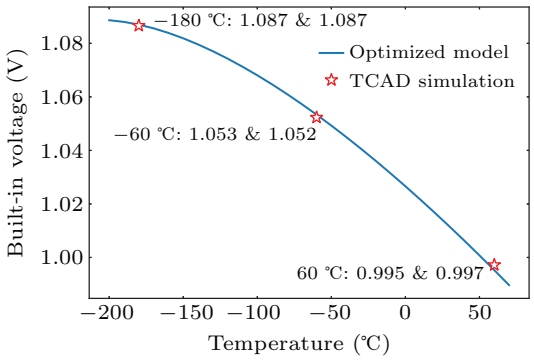


Fig. 16. The built-in voltages of the E/B junction at different temperatures by using the optimized model calculation (blue line and font) and TCAD simulation (red symbols and font).

When the E/B bias is zero ($V_{\rm BE} = 0$ V), one can see there is little electron injection from the emitter to the base because the potential barriers at the E/B junction remain at a high level at almost all temperature points. When $V_{\rm BE} = 0.7$ V, this forward base bias could pull down the E/B barriers by about 0.7 V; at this point, the difference between the E/B barriers with different temperatures comes to the fore. Finally, more electrons are accepted (green arrows in Fig. 15), injected from the emitter to the base at relatively higher temperatures due to the relatively lower barrier height.

In a word, our optimized built-in voltage model could extend the temperature range of the original HICUM model to extremely low temperatures.

5. Summary and conclusion

In this paper, the temperature dependence of single-event transients in SiGe HBTs was investigated. Comparing the experimental data and TCAD simulation results, we found that the variation of carrier mobility with temperature always plays a key role in SET peaks, and the impurity's i.i. will also dominate and make an inflection point when it comes to cryogenic temperatures. These two factors together lead to a significant change in the resistivity of the intrinsic base region and the light-doped collector (both close to the Mott transition). What is more, the novel electron injection from the emitter to the base (when the transistor is in the on-state) will be significantly suppressed at cryogenic temperatures. This phenomenon is mainly due to the high emitter/base junction's barrier heights at low temperatures. An optimized built-in voltage model is proposed to extend the original HICUM model to extremely low temperatures. The present work has provided new evidence for the adaptability and reliability of the SiGe HBT in cryogenic environments.

More work is necessary to improve the convergence of the 3D process simulation at cryogenic temperatures. The cryogenic experimental system needs to be further optimized, especially by thinning the thickness of the quartz window and adding focusing lenses as needed. What is more, we need to study a more accurate simulation method to extract the parasitic series resistance based on the 3D model.

Acknowledgements

The authors want to thank the contributions of the Institute of Microelectronics, Tsinghua University, for providing the DUT in this work. Sun Yabin and Fu Jun have also provided many valuable suggestions on the process simulation. Furthermore, the authors are very grateful to the engineers of SPELS and EKSPLA for their technical support in the daily use of the laser system.

Project supported by the National Natural Science Foundation of China (Grant Nos. 61704127 and 11775167).

References

[1] Cressler J D 2010 *IEEE Transactions on Device and Materials Reliability* **10** 437
[2] Lourenco N E, Fleetwood Z E, Ildefonso A, Wachter M T, Roche N J H, Khachatrian A, McMorrow D, Buchner S P, Warner J H, Itsuji H, Kobayashi D, Hirose K, Paki P, Raman A and Cressler J D 2017 *IEEE Trans. Nucl. Sci.* **64** 406
[3] Sutton A, Moen K, Cressler J D, Carts M, Marshall P, Pellish J, Ramachandran V, Reed R, Alles M and Niu G 2008 *Solid-State Electronics* **52** 1652
[4] Laird J S, Hirao T, Onoda S, Mori H and Itoh H 2002 *IEEE Trans. Nucl. Sci.* **49** 1389
[5] Laird J S, Onoda S and Hirao T 2008 *J. Appl. Phys.* **104** 084510
[6] Ramachandran V, Gadlage M, Ahlbin J, Narasimham B, Alles M, Reed R, Bhuva B, Massengill L, Black J and Foster C 2010 *Solid-State Electronics* **54** 1052
[7] Xu Z, Niu G, Luo L, Cressler J D, Alles M L, Reed R, Mantooth H A, Holmes J and Marshall P W 2010 *IEEE Trans. Nucl. Sci.* **57** 3206
[8] Knudson A R, Campbell A B, Hauser J R, Jessee M, Stapor W J and Shapiro P 1986 *IEEE Trans. Nucl. Sci.* **33** 1560
[9] Schröter M and Chakravorty A 2010 *Compact Hierarchical Bipolar Transistor Modeling With HiCUM* (Singapore: World Scientific) p. 752
[10] Laird J S, Hirao T, Mori H, Onoda S, Kamiya T and Itoh H 2001 *NIMPB* **181** 87
[11] Melinger J S, Buchner S, McMorrow D, Stapor W J, Weatherford T R, Campbell A B and Eisen H 1994 *IEEE Trans. Nucl. Sci.* **41** 2574
[12] Hales J M, Cressler J D, McMorrow D, Khachatrian A, Buchner S, Warner J, Ildefonso A, Tzintzarov G N, Nergui D, Monahan D M and Lalumondiere S D 2020 *IEEE Trans. Nucl. Sci.* **67** 81
[13] Svantesson K G and Nilsson N G 1979 *Journal of Physics C: Solid State Physics* **12** 3837
[14] Zacharias M and Kelires P C 2020 *Phys. Rev. B* **101** 245122
[15] Laird J S, Chen Y, Scheick L, Vo T and Johnston A 2008 *Rev. Sci. Instrum.* **79** 083705
[16] Pan X, Guo H, Feng Y, Liu Y, Zhang J, Li Z, Luo Y, Zhang F, Wang T, Zhao W, Ding L and Xu J 2022 *Science China Technological Sciences* **65** 1193
[17] Palomo F R, Mogollon J M, Napoles J and Aguirre M A 2010 *IEEE Trans. Nucl. Sci.* **57** 1884
[18] Pouget V, Lapuyade H, Fouillat P, Lewis D and Buchner S 2001 *Microelectronics Reliability* **41** 1513
[19] Buchner S P, Miller F, Pouget V and McMorrow D P 2013 *IEEE Trans. Nucl. Sci.* **60** 1852
[20] Hales J M, Khachatrian A, Buchner S, Roche N J H, Warner J, Fleetwood Z E, Ildefonso A, Cressler J D, Ferlet-Cavrois V and McMorrow D 2018 *IEEE Trans. Nucl. Sci.* **65** 1724
[21] Pires R G, Dickstein R M, Titcomb S L and Anderson R L 1990 *Cryogenics* **30** 1064
[22] Loveless T D, Reising D R, Cancelleri J C, Massengill L W and McMorrow D 2021 *IEEE Trans. Nucl. Sci.* **68** 1600
[23] Klaassen D B M 1992 *Solid State Electronics* **35** 961
[24] Jacoboni C, Canali C, Ottaviani G and Alberigi Quaranta A 1977 *Solid-State Electronics* **20** 77
[25] Slotboom J W and de Graaff H C 1976 *Solid State Electronics* **19** 857
[26] Herbert D C 1996 *Fundamentals of Semiconductors: Physics and Materials Properties*, Vol. **11** p. 018
[27] Dash W C and Newman R 1955 *Phys. Rev.* **99** 1151
[28] Zhang J X, He C H, Guo H X, Li P, Guo B L and Wu X X 2017 *Chin. Phys. B* **26** 088502
[29] Khachatrian A, Roche N J H, Dodds N A, McMorrow D, Warner J H, Buchner S P and Reed R A 2015 *IEEE Trans. Nucl. Sci.* **62** 2452
[30] Altermatt P P, Schenk A and Heiser G 2006 *J. Appl. Phys.* **100** 113714
[31] Altermatt P P, Schenk A, Schmithüsen B and Heiser G 2006 *J. Appl. Phys.* **100** 113715
[32] Luo L, Niu G, Moen K A and Cressler J D 2009 *IEEE Trans. Electron Devices* **56** 2169
[33] Mott N F 1968 *Rev. Mod. Phys.* **40** 677
[34] Rosling M, Bleichner H, Jonsson P and Nordlander E 1994 *J. Appl. Phys.* **76** 2855
[35] Dhariwal S R and Ojha V N 1982 *Solid-State Electronics* **25** 909